NANO LETTERS

pubs.acs.org/NanoLett Letter

Double Superconducting Dome of Quasi Two-Dimensional TaS_2 in Non-Centrosymmetric van der Waals Heterostructure

Limin Yan, Kejun Bu, Zhongyang Li, Zihan Zhang, Wei Xia, Mingtao Li, Nana Li, Jiayi Guan, Xuqiang Liu, Jiahao Ning, Dongzhou Zhang, Yanfeng Guo,* Xin Wang,* and Wenge Yang*

Cite This: *Nano Lett.* 2024, 24, 6002−6009 Read Online

ABSTRACT: Two-dimensional van der Waals heterostructures (2D-vdWHs) based on transition metal dichalcogenides (TMDs) provide unparalleled control over electronic properties. However, the interlayer coupling is challenged by the interfacial misalignment and defects, which hinders a comprehensive understanding of the intertwined electronic orders, especially superconductivity and charge density wave (CDW). Here, by using pressure to regulate the interlayer coupling of non-centrosymmetric 6*R*-TaS_2 vdWHs, we observe an unprecedented phase diagram in TMDs. This phase diagram encompasses successive suppression of the original CDW states from alternating *H*-layer and *T*-layer configurations, the emergence and disappearance of a new CDW-like state, and a double superconducting dome induced by different interlayer coupling effects. These results not only illuminate the crucial role of interlayer coupling in shaping the complex phase diagram of TMD systems but also pave a new avenue for the creation of a novel family of bulk heterostructures with customized 2D properties.

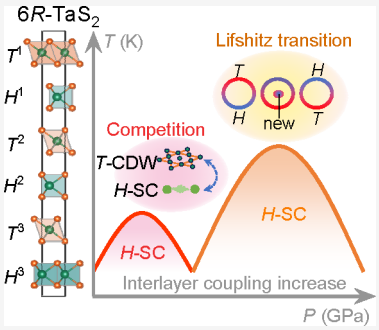

KEYWORDS: *two-dimensional van der Waals heterostructures, charge density wave, superconductivity, double superconducting dome, high pressure, 6R-TaS_2*

Two-dimensional (2D) materials offer a significant platform for creating vertically tailor-made van der Waals heterostructures (vdWHs). The diverse interlayer coupling in vdWHs, which includes a plethora of 2D material choices,[1,2] tunable stacking angles between layers,[3−5] and variations in layer thickness,[6] offers unprecedented desired properties and exotic phenomena.[3,7−10] Thereinto, 2D MX_2 (M = V, Nb, Ta, Ti and X = S, Se, Te) transition metal dichalcogenides (TMDs) exhibit diverse superconductivity and charge density wave (CDW) states,[1,11] making them ideal prototypes for studying the interaction between collective electronic states,[12,13] akin to the situation in unconventional superconductors.[14,15] However, due to interfacial misalignment and defects,[16−18] the investigation into tuning the interlayer coupling of 2D-vdWHs is limited. Achieving a profound comprehension requires appropriate stable materials, along with effective tuning knobs and diagnostic tools to adjust interlayer coupling and consequently modify the superconductivity and CDW states in a controllable manner.

Recent intensive studies of natural bulk vdWH TMDs[19−25] have drawn great attention, as they have been reported to exhibit many novel physical properties such as chiral superconductivity,[19] topological superconductivity,[20] and spontaneous vortices.[21] More importantly, the properties of superconductivity and CDW states in bulk vdWHs have been demonstrated to closely resemble those of their corresponding 2D-vdWHs.[22] Additionally, the superconductivity and CDW states of bulk vdWHs are dependent on factors such as stacking sequence order[22,23] and chemical components,[23,25] providing an exciting opportunity to uncover how different types of interlayer coupling influence these states. High pressure has been utilized as a clean and effective tool for modulating interlayer coupling, thereby leading to the emergence or re-enhancement of superconductivity.[26−33] The emergence of the superconducting dome is generally regarded as the signal of competing and intertwined orders, such as CDW order,[34] orbital order,[35] and magnetic order.[36] The pictures of superconductivity competing and intertwining with CDW order in TMD systems might extend to understanding the behaviors of unconventional superconductivity.

Here, combining *in situ* high-pressure electrical transport measurements, Hall effect measurements, synchrotron X-ray diffraction (XRD), and the first-principles calculations, we systematically investigate the pressure−temperature ($P-T$) phase diagram of non-centrosymmetric 6*R*-TaS_2 constructed by alternately stacking *H*- and *T*-layers up to 53.3 GPa. The observed double superconducting dome phase diagram in

Received: February 1, 2024
Revised: May 8, 2024
Accepted: May 8, 2024
Published: May 13, 2024

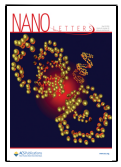

https://doi.org/10.1021/acs.nanolett.4c00579
Nano Lett. 2024, 24, 6002−6009

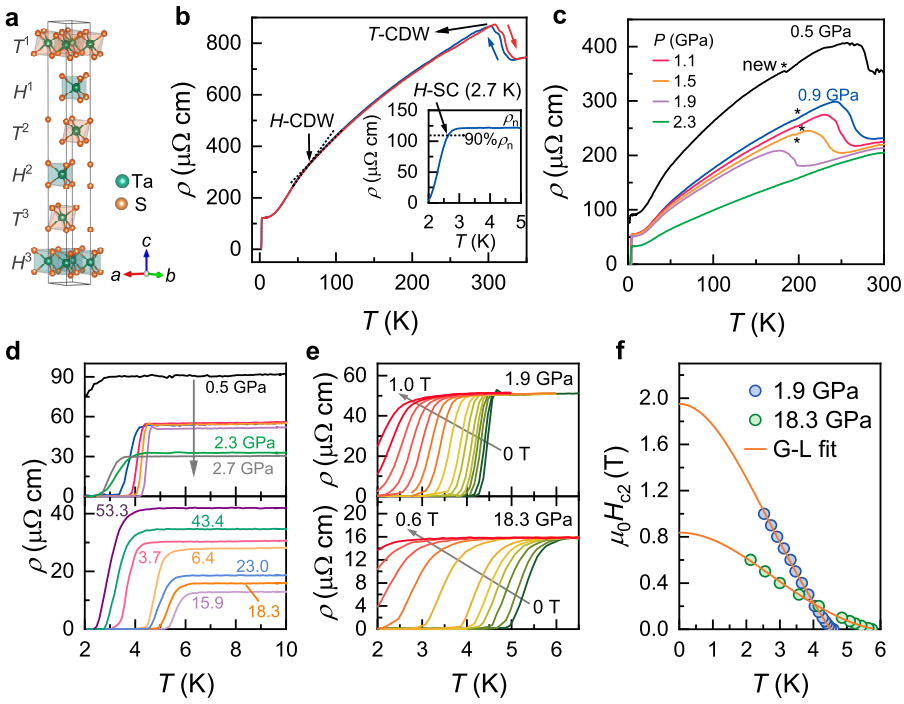

Figure 1. Crystal structure and electrical transport measurements of 6*R*-TaS_2 at various pressures. (a) The crystal structure of 6*R*-TaS_2, consisting of alternately stacked octahedral (*T*) and trigonal prismatic (*H*) layers. (b) The $\rho(T)$ profiles of 6*R*-TaS_2 in the warming (red curve) and cooling (blue curve) processes at ambient pressure. The inset presents the zoomed-in view of the superconducting transition in the temperature range of 2−5 K. Here, the T_c is defined by the resistivity criterion of $\rho_c = 90\%\rho_n$, where ρ_n is the normal state resistivity just above its drop. (c) The resistivity of 6*R*-TaS_2 in the temperature range of 2−300 K at different pressures with the star symbols denoting new abnormal kinks observed upon compression. (d) The $\rho(T)$ profiles of 6*R*-TaS_2 in the pressure ranges of 0.5−2.3 GPa (upper panel) and 3.7−53.3 GPa (lower panel). (e) The $\rho(T)$ profiles at different magnetic fields for 1.9 GPa (right to left: 0, 0.01 T, 0.03 T, 0.05 T, 0.07 T, 0.1 T, 0.15 T, 0.2 T, 0.3 T, 0.4 T, 0.5 T, 0.6 T, 0.7 T,0.8 T, 0.9 T, 1.0 T) and 18.3 GPa (right to left: 0, 0.01 T, 0.03 T, 0.05 T, 0.07 T, 0.1 T, 0.2 T, 0.3 T, 0.4 T, 0.5 T, 0.6 T), respectively. (f) Temperature-dependent upper critical field $\mu_0 H_{c2}$ at 1.9 and 18.3 GPa, with the solid lines representing the Ginzburg−Landau (G-L) fitting.[45]

compressed 6*R*-TaS_2 is distinct from our recent work on the dual-layer superconducting phase diagram in centrosymmetric 4*Hb*-$TaSe_2$ (ref 25); this marks the first observation of a double superconducting dome phase diagram in TMD systems. The first superconducting dome is primarily influenced by pressure-induced modulation of the hole-type carrier density and the competition between the *H*-layer superconductivity and *T*-layer CDW states. The second superconducting dome is associated with the topological phase transition of the Fermi surface (namely, the Lifshitz transition[37]) induced by the interaction between the *H*-layer and the *T*-layer. This unique double superconducting dome phase diagram shares similar mechanisms with unconventional superconductors (such as heavy fermions, cuprates, pnictides,[14,15,38] and recently discovered Kagome metals[39,40]). These findings not only highlight the potential for designing novel functional materials with 2D-tailored properties in bulk vdWHs but also open new avenues for studying superconductivity competing or intertwining with different electronic orders within natural bulk vdWHs.

As illustrated in Figure 1a, 6*R*-TaS_2 possesses a space group of *R*3*m* (No. 160), featuring alternate stacking of 1*T*-TaS_2 and 1*H*-TaS_2 layers. The three *T* (or *H*) layers are oriented in the same direction, with each *T* (or *H*) layer sliding by one-third of the lattice constant *a* relative to the adjacent *T* (or *H*) layer. These layers are connected by weak vdW force, forming a bulk 6*R*-TaS_2 heterostructure. Compared with the recently intensively studied centrosymmetric 4*Hb*-TaX_2 (X = S, Se),[23,25,41,42] the inversion symmetry breaking in the *H*-layer of 6*R*-TaS_2 makes it more likely to exhibit properties akin to those of the free-standing monolayer 1*H*-TaS_2. The pristine 6*R*-TaS_2 powder sample underwent examination using a laboratory X-ray diffractometer, confirming its high purity and good crystallinity with *R*3*m* symmetry[22] (see Figure S1). To investigate the electronic properties of the *T*-layer and *H*-layer within 6*R*-TaS_2, we conducted electrical transport measurements in the temperature range of 2−350 K (Figure 1b). A superconducting transition of 6*R*-TaS_2 was observed at ∼2.7 K (compared to 0.6 K for bulk 2*H*-TaS_2 (ref 43), consistent with the superconducting transition temperature (T_c) of monolayer TaS_2 (∼3 K)[44] and recent demonstrations of the 2D nature of superconductivity in 6*R*-TaS_2 (ref 22). The resistivity derivative $d\rho/dT$ (Figure S2) is utilized to ascertain the transition temperature of the CDW (T_{CDW}) phase transition. Above room temperature, two abnormal jumps in resistivity are observed at ∼320 K (referred to as *T*-CDW[1]) and ∼305 K (*T*-CDW[2]), as shown in Figure 1b, corresponding to two local minima in Figure S2a. These abnormal resistivity signatures are consistent with the recent reports on two CDW transitions originating from the *T*-layer in 6*R*-TaS_2 (ref 22): an incommensurate CDW (ICCDW) to a nearly commensurate CDW (NCCDW) transition at ∼320 K and a NCCDW to a commensurate CDW (CCDW) transition at ∼305 K,[22] respectively. Additionally, the rapid drop in the $\rho(T)$ curve is observed at ∼65.8 K in Figure 1b (an upturn of $d\rho/dT$ in Figure S2b). This behavior of resistivity with temperature closely resembles the CDW transition observed in 2*H*-TaS_2 at ∼76 K (ref 11), hereinafter referred to as *H*-CDW.

https://doi.org/10.1021/acs.nanolett.4c00579
Nano Lett. 2024, 24, 6002−6009

To investigate the interplay between the superconductivity and multiple CDW states in 6*R*-TaS_2, we have performed the *in situ* high-pressure electrical transport measurements on single-crystal flakes in the temperature range of 2−300 K. From the $\rho(T)$ curves at various pressures illustrated in Figure 1c, both an upturn (T-CDW^1 and T-CDW^2) and rapid drop (H-CDW) of resistivity are suppressed by pressure and quickly shift to the lower temperature range. Remarkably, a new kink of resistivity first appears at ∼185 K from the $\rho(T)$ curve at 0.5 GPa, which resembles the CDW-like phase transition (referred to as a new state), and it persists up to 1.9 GPa. The T_c (Figure 1d) initially increases with pressure up to 4.6 K at 1.9 GPa, followed by a sharp drop until 2.7 GPa ($T_c \sim 3.2$ K). Then T_c subsequently increases to a maximum of 6 K at 15.9 GPa and falls back slowly once again. Figure 1e displays the $\rho(T)$ curves at different magnetic fields for 1.9 and 18.3 GPa, and the corresponding $\mu_0 H_{c2}$ as a function of the critical temperature T_c is given in Figure 1f, which can be well characterized by the Ginzburg−Landau (G-L) fittings.[45] It is noteworthy that the $\mu_0 H_{c2}(T)$ data follow a single G-L fitting curve rather than two for each pressure, indicating the T-layer of 6*R*-TaS_2 does not enter superconductivity (at least above 2 K). This distinguishes it from the pressure-induced dual-layer superconductivity observed in 4*Hb*-$TaSe_2$ (ref 25). The transition temperatures of CDW states from the T-layer and H-layer, along with the CDW-like new state (see Figure S2), are analyzed and plotted together with T_c in the phase diagram shown in Figure 2.

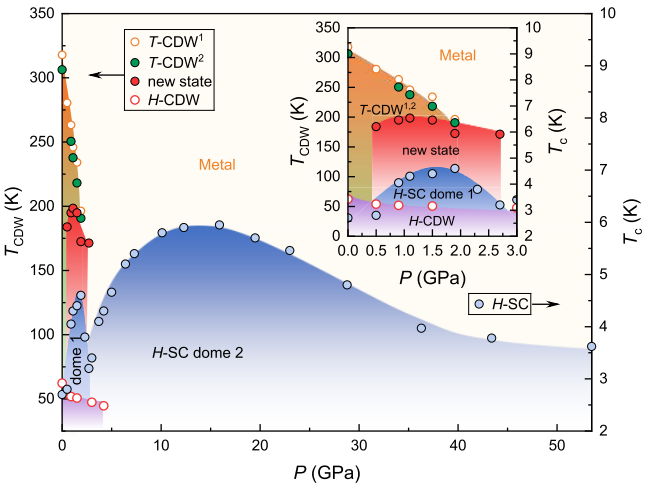

Figure 2. Pressure−temperature phase diagram of 6*R*-TaS_2. The inset is an enlarged view of the phase diagram in the pressure range of 0−3 GPa.

As illustrated in Figure 2, there are two superconducting domes at 0−3 GPa and 3−53.3 GPa, respectively. In the regime of the first superconducting dome, T_c maximizes to 4.6 K at 1.9 GPa, where both T-CDW^1 and T-CDW^2 are suppressed by pressure, indicating a strong competition between the H-layer superconductivity and T-layer CDW states. This competition between superconductivity and CDW states from different types of layers has also been observed in the 4*Hb*-$TaSe_2$ heterostructure.[25] Differently, the T-layer of 4*Hb*-$TaSe_2$ enters a superconducting state at ∼9 GPa, forming dual-layer superconductivity, while the T-layer of 6*R*-TaS_2 does not exhibit any signature of the superconductivity within the pressure range in this work (0−53.3 GPa). Furthermore, the pressure-induced emergence and disappearance of a new CDW-like state in 6*R*-TaS_2 has not been observed in compressed 4*Hb*-$TaSe_2$. More importantly, previous phase diagrams reported in 1*T*- and 2*H*-TMDs merely possess one superconducting dome therein.[28,30,46] The double superconducting dome observed in 6*R*-TaS_2 has commonly been observed in unconventional superconductors,[14,15,38−40] in which the formation of a double superconducting dome is associated with a quantum critical point (QCP),[47] non-Fermi liquid (NFL),[14] Lifshitz transition,[38] or modification of the CDW order.[40] Notably, the tendency of $T_{CDW}(P)$ of the CDW-like new state within 6*R*-TaS_2 is quite consistent with the $T_c(P)$ below 3 GPa, suggesting that this state may be intertwined with the superconductivity, as in the Kagome superconductor reported in CsV_3Sb_5 (ref 40). But the origin of this new state is unclear and needs further investigation.

To gain insight into the double superconducting dome of 6*R*-TaS_2, we analyze the $\rho(T)$ curves of the normal state with an empirical formula $\rho = \rho_0 + AT^n$ at $T_c < T \leq 30$ K. Here, ρ_0 represents the residual resistivity contributed from impurity scattering, A is the prefactor, and n is the exponential parameter. The fitting results are shown in Figure S3. In the first superconducting dome region, the $n(P)$ profile (Figure 3a) shows a dip at 1.5 GPa, coinciding with a peak of the $A(P)$ profile (Figure 3b), which agrees with the fact that the T_c forms a dome shape accompanied by suppression of both T-CDW^1 and T-CDW^2. These behaviors are very similar to those observed in cases of the quantum fluctuation induced by the suppression of the CDW states in the TMD systems.[28,30,46] It should be noticed that the H-layer CDW can survive until 6.4 GPa; thus, the first superconducting dome of 6*R*-TaS_2 is majorly associated with the competition between the CDW state of the T-layer and the superconductivity of the H-layer.

To investigate the possible electronic structure phase transition and the origin of the double superconducting dome of 6*R*-TaS_2, we first performed Hall effect measurements. The Hall resistances R_{xy} as a function of the magnetic field at different pressures are presented in Figure S4.

At ambient pressure, the $R_{xy}(H)$ data at 2 and 10 K show a nonlinear trend, similar to the alternately stacked 4*Hb*-TaS_2 (ref 23). However, its nonlinear behavior rapidly changes to a linear trend above 0.9 GPa, as shown in Figure S4, and the slope of the $R_{xy}(H)$ changes from positive to negative at a critical pressure of 15.9 GPa. The pressure-dependent Hall coefficient R_H extracted from the slope of the $R_{xy}(H)$ curves (Figure S4) in the pressure range of 0.9−30 GPa is plotted in Figure 3c.

The positive Hall coefficient R_H indicates that the hole-type carrier dominates the transport behavior for $0.9 \leq P < 15.9$ GPa. In this pressure range, the R_H rapidly increases below 3 GPa, followed by a gradual increase in the pressure range of 3−5 GPa. However, the R_H sharply decreases with pressure beyond 5 GPa until 10 GPa. Eventually, the R_H changes its sign from positive to negative at 15.9 GPa, indicating a shift from hole-type to electron-type carriers at the Fermi surface. We also estimated the effective carrier concentration n_H ($= 1/|e \times R_H|$) with pressure, as displayed in Figure 3d. Surprisingly, the carrier density as a function of pressure shows a pronounced change at ∼2 GPa (the inset in Figure 3d). Furthermore, the ratio of $(-dH_{c2}/dT|_{T=T_c})/T_c$ ($\propto 1/v_F^2$, where v_F is the Fermi velocity)[48] (shown in Figure S5) initially increases with pressure until 2.7 GPa but rapidly decreases, indicating a modulation of the electronic structure around 3 GPa, which is

https://doi.org/10.1021/acs.nanolett.4c00579
Nano Lett. 2024, 24, 6002−6009

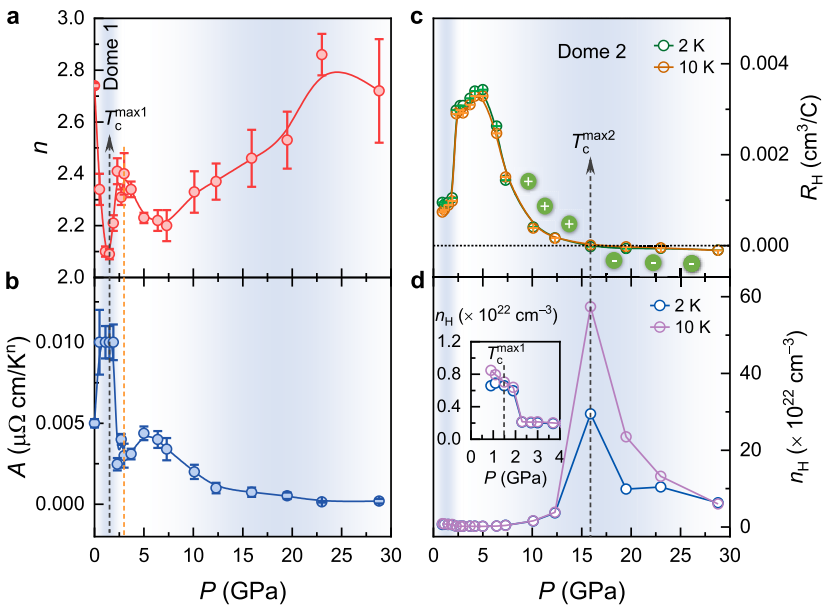

Figure 3. Analysis of the normal resistance and the Hall effect measurements on 6*R*-TaS_2. (a and b) Pressure-dependent refined parameters *A* and *n* (based on the equation $\rho = \rho_0 + AT^n$, where ρ_0 is the residual resistivity and *A* and *n* are the coefficient and exponent of temperature), respectively. The fitting results are presented in Figure S3. The orange dashed line at 3 GPa is a guide to the eye. (c and d) Hall coefficient and carrier density as a function of pressure, respectively.

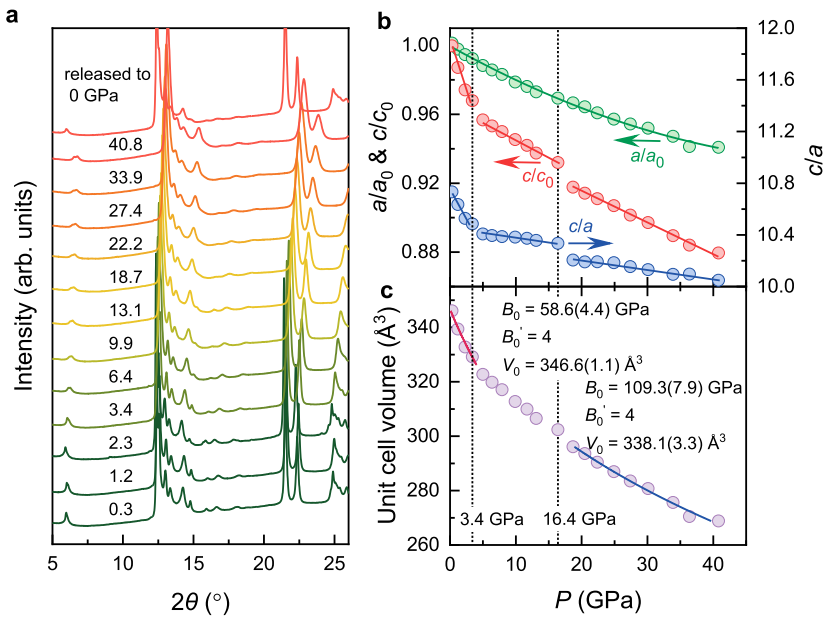

Figure 4. High-pressure synchrotron XRD measurements of 6*R*-TaS_2. (a) Representative powder XRD patterns between 0.3 and 40.8 GPa. (b) Pressure-dependent normalized compression ratio a/a_0 and c/c_0 (left) and c/a (right) extracted from powder diffraction Rietveld refinements. The solid lines are guides for the eyes. (c) Pressure-dependent unit-cell volume. Solid lines are the fitting curves with the Birch−Murnaghan equation of state.[52]

concomitant with the re-enhancement of the *H*-layer superconductivity, as shown in Figure 2. As the pressure increases, the carrier density n_H increases by 2 orders of magnitude and reaches a maximum value at 15.9 GPa. Meanwhile, T_c reaches the highest value in the second superconducting dome (see Figure 2). Beyond 15.9 GPa, the dominant carrier type is changed to electron type, accompanied by a rapid decrease in carrier density. These behaviors suggest 6*R*-TaS_2 may undergo a Lifshitz transition at ∼15.9 GPa, consequently dominating the second superconducting dome.

Pressure can not only modulate electronic structure effectively but also induce crystal structural phase transition, such as layer sliding and interlayer bonding, which consequently influence the properties of superconductivity.[31,49−51] To assess the structural evolution of 6*R*-TaS_2 under pressure, we performed *in situ* high-pressure synchrotron XRD measurements at the Advanced Photon Source. Figure 4a presents the selected XRD patterns between 0.3 and 40.8 GPa. All diffraction peaks shift to higher angle during compression, and no new peaks are observed, indicating that 6*R*-TaS_2 retains its ambient crystallographic symmetry. However, detailed

https://doi.org/10.1021/acs.nanolett.4c00579
Nano Lett. 2024, 24, 6002−6009

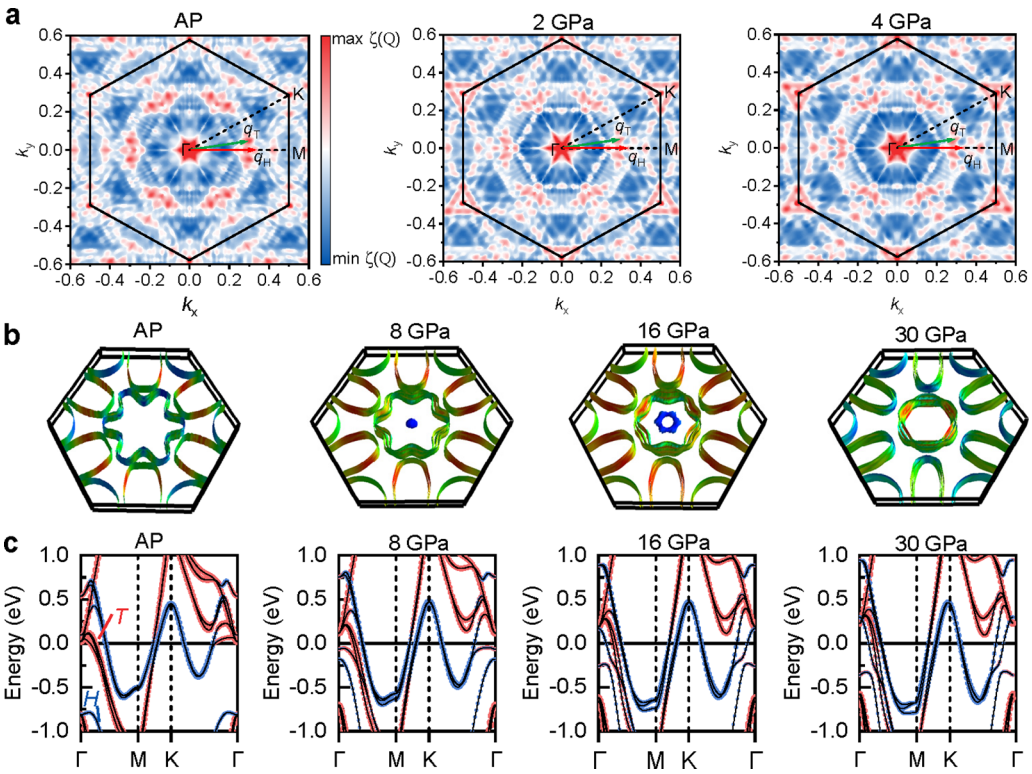

Figure 5. Calculated Fermi surface nesting conditions, Fermi surface, and projected band structures of 6*R*-TaS_2. (a) The nesting function without spin−orbit coupling of 6*R*-TaS_2 at ambient pressure, 2 GPa, and 4 GPa, respectively. The highest value of the color bar corresponds to 30% of the intensity of the gamma point, and the lowest value of the color bar represents the minimum value of the real intensity. (b) The Fermi surface without spin−orbit coupling of the 6*R*-TaS_2 at ambient pressure and 8, 16, and 30 GPa, respectively. (c) The corresponding projected band structures without spin−orbit coupling. The blue and red data points denote the spectral weights contributed by the *H*-layer and *T*-layer, respectively.

analysis of the lattice parameters (Figure 4b) and unit cell volume (Figure 4c) reveals two isostructural phase transitions (iSPTs) occurred at 3.4 and 16.4 GPa, respectively. The normalized compression ratio a/a_0 continuously decreases with pressure, in stark contrast to the normalized compression ratio c/c_0 with two discontinuities at 3.4 and 16.4 GPa, respectively. This indicates that interlayer coupling plays a significant role in the structural changes. It should be noticed that the ratio of c/a presented in Figure 4b (right *y*-axis) rapidly decreases in the pressure range of 0−3.4 GPa and suddenly becomes robust and exhibits a flattened trend in the second pressure range (3.4−16.4 GPa). This evolution indicates a transformation from the original quasi-2D structure to a quasi-3D lattice. And consequently, the initial quasi-2D superconductivity may develop into a 3D superconductivity. While the further systematic characterization of high-pressure 2D superconductivity is warranted, it has not been explored in this study. Furthermore, the normal resistivity at 10 K also shows two discontinuities at 3.4 and 15.9 GPa (see Figure S6), indicating 6*R*-TaS_2 undergoes two iSPTs. These two critical pressures of the c/a ratio discontinuities are well consistent with the above Hall effect measurements, indicating a strong correlation between the crystal structure and electronic properties.

As shown in Figure 4c, the fitting with the second-order (B_0' = 4.0) Birch−Murnaghan equation of state[52] yields two bulk moduli for 0.3 GPa $\leq P \leq$ 3.4 and 16.5 GPa $\leq P \leq$ 40.8 GPa, respectively. Several recent works in TMD systems have also shown that the iSPT may be induced by the electronic topological phase transition (or so-called Lifshitz phase transition[37]), and the properties of superconductivity are highly related to such transition.[50,53] As shown in Figure 4a, these iSPTs are reversible after fully releasing the applied pressure.

Next, to elucidate the behavior of the suppression of CDW states from different layers, the observed electronic structural modulation, and the double superconducting domes within the phase diagram of 6*R*-TaS_2, we calculated the Fermi surface nesting conditions (below 4 GPa), Fermi surface (0−40 GPa), and electronic band structure (0−40 GPa) for undistorted 6*R*-TaS_2 using the first-principles calculations. The Fermi surface nesting is thought to be one of the driving forces of the CDW order.[54,55] If the CDW order originates from the Fermi-surface nesting, a maximum value of nesting function $\xi(Q)$ will appear at q_{CDW} in the Brillouin zone.[56,57] Thus, we calculated the Fermi surface nesting function in the 6*R*-TaS_2 based on the formula

$$\xi(Q) = \frac{1}{N}\sum_{\boldsymbol{k},i,j} \delta(\varepsilon_{\mathrm{k},i} - \varepsilon_{\mathrm{F}}) \times \delta(\varepsilon_{\boldsymbol{k}+Q,j} - \varepsilon_{\mathrm{F}})$$

where the ε_k represents the Kohn−Sham eigenvalue, ε_F is the Fermi level, and i and j are the indices of the energy bands, respectively. As shown in Figure 5a, at ambient pressure, there are two maxima around the positions of $q_H \sim \frac{1}{3}a^*$ (red arrows for the *H*-layer) and $q_T \sim 0.297a^* + 0.049b^*$ (green arrows for monolayer *T*-layer), which are consistent with reported 2*H*-TaS_2 (ref 58) and 1*T*-TaS_2 (ref 59), respectively. The nesting

https://doi.org/10.1021/acs.nanolett.4c00579
Nano Lett. 2024, 24, 6002−6009

intensities located at the q_{CDW} are suppressed upon compression and almost disappear at 4 GPa, indicating the suppression of the CDW states. This result is qualitatively consistent with the electrical transport measurements shown in Figure 1c. Thus, the variation tendency of CDW temperature of both the *T*-layer and *H*-layer in 6*R*-TaS_2 is consistent with that of Fermi surface nesting strength as pressure increases, suggesting that the emergence of CDW states was caused by Fermi surface nesting of both the *T*-layer and *H*-layer in 6*R*-TaS_2.

To confirm the Lifshitz transition of 6*R*-TaS_2 at ∼15.9 GPa, as indicated by the change in Hall coefficient sign and the rapid decrease in carrier density (Figure 3c and d), we also calculated the Fermi surface of the 6*R*-TaS_2 under high pressures (see Figure 5b). An additional hole pocket emerges around the Γ point at 8 GPa, then transforms from a pancake to a torus upon further compression (see Figure 5b and Figure S7), but somehow disappears at $P > 16$ GPa. The further calculations on the projected band structures presented in Figure 5c and Figure S8 have shown that the emergence and the disappearance of the new hole pocket around the Γ point are induced by the band shift and inversion between the *T*-layer and *H*-layer. Therefore, combining the results from theory and experiment, we can draw a conclusion that 6*R*-TaS_2 indeed undergoes a Lifshitz transition at ∼16 GPa. Returning to the phase diagram in Figure 2, coincidently, we notice that the peak of the second superconducting dome is also located at ∼16 GPa. Therefore, this Lifshitz phase transition dominates the second superconducting dome.

In summary, we comprehensively investigate the *P*−*T* phase diagram of 6*R*-TaS_2 through a combination of *in situ* high-pressure experiments and theoretical calculations. We discovered a double superconducting dome with distinct mechanisms: one dome arises from the competition between the *H*-layer superconductivity and *T*-layer CDW states, while the other, with higher T_c, is dominated by a Lifshitz transition induced by the *H*-layer and *T*-layer interaction. The distinctive phase diagram of 6*R*-TaS_2 not only paves the way for a deeper understanding of the intricate relationship between superconductivity and charge density wave, extending insights to unconventional superconductivity featuring a similar double superconducting dome, but also establishes a viable approach to unravel interlayer coupling in diverse layered materials. Moreover, it offers valuable guidance for the future design of CDW-based bulk vdHWs materials with 2D customized properties.

■ ASSOCIATED CONTENT

Supporting Information

The Supporting Information is available free of charge at https://pubs.acs.org/doi/10.1021/acs.nanolett.4c00579.

Materials and methods; preparation and characterization of 6*R*-TaS_2, electrical transport measurements, Hall effect measurements, and first-principles calculations (PDF)

■ AUTHOR INFORMATION

Corresponding Authors

Yanfeng Guo − *School of Physical Science and Technology and ShanghaiTech Laboratory for Topological Physics, ShanghaiTech University, Shanghai 201210, People's Republic of China;* orcid.org/0000-0002-9386-4857; Email: guoyf@shanghaitech.edu.cn

Xin Wang − *State Key Laboratory of Superhard Materials, Department of Physics, Jilin University, Changchun 130012, People's Republic of China*; Email: xin_wang@jlu.edu.cn

Wenge Yang − *Center for High Pressure Science and Technology Advanced Research (HPSTAR), Shanghai 201203, People's Republic of China;* orcid.org/0000-0001-8436-8731; Email: yangwg@hpstar.ac.cn

Authors

Limin Yan − *Center for High Pressure Science and Technology Advanced Research (HPSTAR), Shanghai 201203, People's Republic of China; School of Science, Inner Mongolia University of Science and Technology, Baotou 014010, People's Republic of China; State Key Laboratory of Superhard Materials, Department of Physics, Jilin University, Changchun 130012, People's Republic of China*

Kejun Bu − *Center for High Pressure Science and Technology Advanced Research (HPSTAR), Shanghai 201203, People's Republic of China;* orcid.org/0000-0002-1466-2764

Zhongyang Li − *School of Physical Science and Technology, ShanghaiTech University, Shanghai 201210, People's Republic of China; Center for High Pressure Science and Technology Advanced Research (HPSTAR), Shanghai 201203, People's Republic of China*

Zihan Zhang − *State Key Laboratory of Superhard Materials, Department of Physics, Jilin University, Changchun 130012, People's Republic of China*

Wei Xia − *School of Physical Science and Technology and ShanghaiTech Laboratory for Topological Physics, ShanghaiTech University, Shanghai 201210, People's Republic of China*

Mingtao Li − *Center for High Pressure Science and Technology Advanced Research (HPSTAR), Shanghai 201203, People's Republic of China*

Nana Li − *Center for High Pressure Science and Technology Advanced Research (HPSTAR), Shanghai 201203, People's Republic of China*

Jiayi Guan − *Center for High Pressure Science and Technology Advanced Research (HPSTAR), Shanghai 201203, People's Republic of China; School of Physics, Beijing Institute of Technology, Beijing 100081, People's Republic of China*

Xuqiang Liu − *Center for High Pressure Science and Technology Advanced Research (HPSTAR), Shanghai 201203, People's Republic of China*

Jiahao Ning − *Center for High Pressure Science and Technology Advanced Research (HPSTAR), Shanghai 201203, People's Republic of China*

Dongzhou Zhang − *GSECARS, University of Chicago, Argonne, Illinois 60439, United States;* orcid.org/0000-0002-6679-892X

Complete contact information is available at: https://pubs.acs.org/10.1021/acs.nanolett.4c00579

Author Contributions

L.Y., K.B., and Z.L. contributed equally to this project. W.Y. and X.W. conceived and designed the project. L.Y., Z.L., W.X., and Y.G. synthesized the crystals. L.Y. performed high-pressure electrical transport, Hall effect, and XRD measurements. N.L., J.G., X.L., and D.Z. assisted with conducting the high-pressure XRD measurements. M.L. and J.N. helped to perform the electrical transport measurements and analysis of the electrical

transport data. K.B. and Z.Z. performed the first-principles calculations. All authors contributed to the discussion of the results and revision of the manuscript.

Funding

This work was supported by the National Nature Science Foundation of China under Grant Nos. U2230401, 12204022, and 11804011. X.L. was supported by the National Postdoctoral Foundation Project of China under Grants No. GZC20230215. Y.G. acknowledges the National Key R & D Program of China (Grant No. 2023YFA1406100) and the open project from State Key Laboratory of Functional Materials for Informatics (Grant No. SKL2022), CAS.

Notes

The authors declare no competing financial interest.

■ ACKNOWLEDGMENTS

In situ high-pressure X-ray diffraction measurements were performed at Sector 13, Advanced Photon Source (APS), Argonne National Laboratory. GeoSoilEnviroCARS is supported by the National Science Foundation-Earth Sciences (EAR-1634415) and the Department of Energy-GeoSciences (DE-FG02-94ER14466). The Advanced Photon Source, a U.S. Department of Energy (DOE) Office of Science User Facility, is operated for the DOE Office of Science by Argonne National Laboratory under Contract No. DE-AC02-06CH11357. Partial XRD work was completed at the 15U1 station, Shanghai Synchrotron Radiation Facility (SSRF), Zhangjiang Lab, and the BL10-XU station at Spring-8. We appreciate the technical support of Drs. S. Jiang, S. Kawaguchi, and Y. Ohishi. The authors acknowledge the financial support from Shanghai Science and Technology Committee, China (No. 22JC1410300) and Shanghai Key Laboratory of Material Frontiers Research in Extreme Environments, China (No. 22dz2260800).

■ ABBREVIATIONS

2D, two-dimensional; vdWHs, van der Waals heterostructures; TMD, transition metal dichalcogenide; CDW, charge density wave; T_c, superconducting transition temperature; T_{CDW}, transition temperature of charge density wave; ICCDW, incommensurate charge density wave; NCCDW, nearly commensurate charge density wave; CCDW, commensurate charge density wave; XRD, X-ray diffraction; iSPT, isostructural phase transition

■ REFERENCES

(1) Zhou, J.; Lin, J.; Huang, X.; Zhou, Y.; Chen, Y.; Xia, J.; Wang, H.; Xie, Y.; Yu, H.; Lei, J.; et al. A library of atomically thin metal chalcogenides. *Nature* **2018**, *556* (7701), 355−359.

(2) Geim, A. K.; Grigorieva, I. V. Van der Waals heterostructures. *Nature* **2013**, *499* (7459), 419−425.

(3) Cao, Y.; Fatemi, V.; Fang, S.; Watanabe, K.; Taniguchi, T.; Kaxiras, E.; Jarillo-Herrero, P. Unconventional superconductivity in magic-angle graphene superlattices. *Nature* **2018**, *556* (7699), 43−50.

(4) Zhao, W.-M.; Zhu, L.; Nie, Z.; Li, Q.-Y.; Wang, Q.-W.; Dou, L.-G.; Hu, J.-G.; Xian, L.; Meng, S.; Li, S.-C. Moiré enhanced charge density wave state in twisted 1*T*-$TiTe_2$/1*T*-$TiSe_2$ heterostructures. *Nat. Mater.* **2022**, *21* (3), 284−289.

(5) Jin, C.; Regan, E. C.; Yan, A.; Iqbal Bakti, U. M.; Wang, D.; Zhao, S.; Qin, Y.; Yang, S.; Zheng, Z.; Shi, S.; et al. Observation of moire excitons in WSe_2/WS_2 heterostructure superlattices. *Nature* **2019**, *567* (7746), 76−80.

(6) Zhou, Z.; Hou, F.; Huang, X.; Wang, G.; Fu, Z.; Liu, W.; Yuan, G.; Xi, X.; Xu, J.; Lin, J.; et al. Stack growth of wafer-scale van der Waals superconductor heterostructures. *Nature* **2023**, *621* (7979), 499−505.

(7) Novoselov, K. S.; Mishchenko, A.; Carvalho, A.; Castro Neto, A. H. 2D materials and van der Waals heterostructures. *Science* **2016**, *353* (6298), aac9439.

(8) Regan, E. C.; Wang, D.; Jin, C.; Bakti Utama, M. I.; Gao, B.; Wei, X.; Zhao, S.; Zhao, W.; Zhang, Z.; Yumigeta, K.; et al. Mott and generalized Wigner crystal states in WSe_2/WS_2 moire superlattices. *Nature* **2020**, *579* (7799), 359−363.

(9) Kezilebieke, S.; Huda, M. N.; Vaňo, V.; Aapro, M.; Ganguli, S. C.; Silveira, O. J.; Głodzik, S.; Foster, A. S.; Ojanen, T.; Liljeroth, P. Topological superconductivity in a van der Waals heterostructure. *Nature* **2020**, *588* (7838), 424−428.

(10) Xia, J.; Yan, J.; Wang, Z.; He, Y.; Gong, Y.; Chen, W.; Sum, T. C.; Liu, Z.; Ajayan, P. M.; Shen, Z. Strong coupling and pressure engineering in WSe_2−$MoSe_2$ heterobilayers. *Nat. Phys.* **2021**, *17* (1), 92−98.

(11) Wilson, J. A.; Di Salvo, F. J.; Mahajan, S. Charge-density waves and superlattices in the metallic layered transition metal dichalcogenides. *Adv. Phys.* **1975**, *24* (2), 117−201.

(12) Ritschel, T.; Trinckauf, J.; Koepernik, K.; Büchner, B.; Zimmermann, M. v.; Berger, H.; Joe, Y. I.; Abbamonte, P.; Geck, J. Orbital textures and charge density waves in transition metal dichalcogenides. *Nat. Phys.* **2015**, *11* (4), 328−331.

(13) Yu, Y.; Yang, F.; Lu, X. F.; Yan, Y. J.; Cho, Y.-H.; Ma, L.; Niu, X.; Kim, S.; Son, Y.-W.; Feng, D.; et al. Gate-tunable phase transitions in thin flakes of 1*T*-TaS_2. *Nat. Nanotechnol.* **2015**, *10* (3), 270−276.

(14) Das, T.; Panagopoulos, C. Two types of superconducting domes in unconventional superconductors. *New J. Phys.* **2016**, *18* (10), No. 103033.

(15) Keimer, B.; Kivelson, S. A.; Norman, M. R.; Uchida, S.; Zaanen, J. From quantum matter to high-temperature superconductivity in copper oxides. *Nature* **2015**, *518* (7538), 179−186.

(16) Rhodes, D.; Chae, S. H.; Ribeiro-Palau, R.; Hone, J. Disorder in van der Waals heterostructures of 2D materials. *Nat. Mater.* **2019**, *18* (6), 541−549.

(17) Liang, Q.; Zhang, Q.; Zhao, X.; Liu, M.; Wee, A. T. S. Defect Engineering of Two-Dimensional Transition-Metal Dichalcogenides: Applications, Challenges, and Opportunities. *ACS Nano* **2021**, *15* (2), 2165−2181.

(18) Dai, Z.; Liu, L.; Zhang, Z. Strain Engineering of 2D Materials: Issues and Opportunities at the Interface. *Adv. Mater.* **2019**, *31* (45), 1805417.

(19) Ribak, A.; Skiff, R. M.; Mograbi, M.; Rout, P. K.; Fischer, M. H.; Ruhman, J.; Chashka, K.; Dagan, Y.; Kanigel, A. Chiral superconductivity in the alternate stacking compound 4*Hb*-TaS_2. *Sci. Adv.* **2020**, *6* (13), eaax9480.

(20) Nayak, A. K.; Steinbok, A.; Roet, Y.; Koo, J.; Margalit, G.; Feldman, I.; Almoalem, A.; Kanigel, A.; Fiete, G. A.; Yan, B.; et al. Evidence of topological boundary modes with topological nodal-point superconductivity. *Nat. Phys.* **2021**, *17* (12), 1413−1419.

(21) Persky, E.; Bjørlig, A. V.; Feldman, I.; Almoalem, A.; Altman, E.; Berg, E.; Kimchi, I.; Ruhman, J.; Kanigel, A.; Kalisky, B. Magnetic memory and spontaneous vortices in a van der Waals superconductor. *Nature* **2022**, *607* (7920), 692−696.

(22) Achari, A.; Bekaert, J.; Sreepal, V.; Orekhov, A.; Kumaravadivel, P.; Kim, M.; Gauquelin, N.; Balakrishna Pillai, P.; Verbeeck, J.; Peeters, F. M.; et al. Alternating Superconducting and Charge Density Wave Monolayers within Bulk 6*R*-TaS_2. *Nano Lett.* **2022**, *22* (15), 6268−6275.

(23) Gao, J. J.; Si, J. G.; Luo, X.; Yan, J.; Jiang, Z. Z.; Wang, W.; Han, Y. Y.; Tong, P.; Song, W. H.; Zhu, X. B.; et al. Origin of the large magnetoresistance in the candidate chiral superconductor 4*Hb*-TaS_2. *Phys. Rev. B* **2020**, *102* (7), No. 075138.

(24) Wen, C.; Gao, J.; Xie, Y.; Zhang, Q.; Kong, P.; Wang, J.; Jiang, Y.; Luo, X.; Li, J.; Lu, W.; et al. Roles of the Narrow Electronic Band near the Fermi Level in 1*T*-TaS_2-Related Layered Materials. *Phys. Rev. Lett.* **2021**, *126* (25), No. 256402.

https://doi.org/10.1021/acs.nanolett.4c00579
Nano Lett. 2024, 24, 6002−6009

(25) Yan, L.; Ding, C.; Li, M.; Tang, R.; Chen, W.; Liu, B.; Bu, K.; Huang, T.; Dai, D.; Jin, X.; et al. Modulating Charge-Density Wave Order and Superconductivity from Two Alternative Stacked Monolayers in a Bulk 4*Hb*-$TaSe_2$ Heterostructure via Pressure. *Nano Lett.* **2023**, *23* (6), 2121−2128.
(26) Morosan, E.; Zandbergen, H. W.; Dennis, B. S.; Bos, J. W. G.; Onose, Y.; Klimczuk, T.; Ramirez, A. P.; Ong, N. P.; Cava, R. J. Superconductivity in Cu_xTiSe_2. *Nat. Phys.* **2006**, *2* (8), 544−550.
(27) Wang, B.; Liu, Y.; Luo, X.; Ishigaki, K.; Matsubayashi, K.; Lu, W.; Sun, Y.; Cheng, J.; Uwatoko, Y. Universal phase diagram of superconductivity and charge density wave versus high hydrostatic pressure in pure and Se-doped 1*T*-TaS_2. *Phys. Rev. B* **2018**, *97* (22), No. 220504.
(28) Kusmartseva, A. F.; Sipos, B.; Berger, H.; Forró, L.; Tutiš, E. Pressure Induced Superconductivity in Pristine 1*T*-$TiSe_2$. *Phys. Rev. Lett.* **2009**, *103* (23), No. 236401.
(29) Freitas, D. C.; Rodière, P.; Osorio, M. R.; Navarro-Moratalla, E.; Nemes, N. M.; Tissen, V. G.; Cario, L.; Coronado, E.; García-Hernández, M.; Vieira, S.; et al. Strong enhancement of superconductivity at high pressures within the charge-density-wave states of 2*H*-TaS_2 and 2*H*-$TaSe_2$. *Phys. Rev. B* **2016**, *93* (18), No. 184512.
(30) Wang, B.; Liu, Y.; Ishigaki, K.; Matsubayashi, K.; Cheng, J.; Lu, W.; Sun, Y.; Uwatoko, Y. Pressure-induced bulk superconductivity in a layered transition-metal dichalcogenide 1*T*-tantalum selenium. *Phys. Rev. B* **2017**, *95* (22), No. 220501.
(31) Dong, Q.; Li, Q.; Li, S.; Shi, X.; Niu, S.; Liu, S.; Liu, R.; Liu, B.; Luo, X.; Si, J.; et al. Structural phase transition and superconductivity hierarchy in 1*T*-TaS_2 under pressure up to 100 GPa. *npj Quantum Mater.* **2021**, *6* (1), 20.
(32) Dong, Q.; Pan, J.; Li, S.; Fang, Y.; Lin, T.; Liu, S.; Liu, B.; Li, Q.; Huang, F.; Liu, B. Record-High Superconductivity in Transition Metal Dichalcogenides Emerged in Compressed 2*H*-TaS_2. *Adv. Mater.* **2022**, *34* (9), 2103168.
(33) Chi, Z.; Chen, X.; Yen, F.; Peng, F.; Zhou, Y.; Zhu, J.; Zhang, Y.; Liu, X.; Lin, C.; Chu, S.; et al. Superconductivity in Pristine 2*Ha*-MoS_2 at Ultrahigh Pressure. *Phys. Rev. Lett.* **2018**, *120* (3), No. 037002.
(34) Yu, F. H.; Ma, D. H.; Zhuo, W. Z.; Liu, S. Q.; Wen, X. K.; Lei, B.; Ying, J. J.; Chen, X. H. Unusual competition of superconductivity and charge-density-wave state in a compressed topological kagome metal. *Nat. Commun.* **2021**, *12* (1), 3645.
(35) Singh, U. R.; White, S. C.; Schmaus, S.; Tsurkan, V.; Loidl, A.; Deisenhofer, J.; Wahl, P. Evidence for orbital order and its relation to superconductivity in $FeSe_{0.4}Te_{0.6}$. *Sci. Adv.* **2015**, *1* (9), e1500206.
(36) Eckberg, C.; Campbell, D. J.; Metz, T.; Collini, J.; Hodovanets, H.; Drye, T.; Zavalij, P.; Christensen, M. H.; Fernandes, R. M.; Lee, S.; et al. Sixfold enhancement of superconductivity in a tunable electronic nematic system. *Nat. Phys.* **2020**, *16* (3), 346−350.
(37) Lifshitz, I. M. Anomalies of electron characteristics of a metal in the high pressure region. *Soviet Physics, JETP.* **1960**, *11*, 1130.
(38) Shimizu, M.; Takemori, N.; Guterding, D.; Jeschke, H. O. Two-Dome Superconductivity in FeS Induced by a Lifshitz Transition. *Phys. Rev. Lett.* **2018**, *121* (13), No. 137001.
(39) Chen, K. Y.; Wang, N. N.; Yin, Q. W.; Gu, Y. H.; Jiang, K.; Tu, Z. J.; Gong, C. S.; Uwatoko, Y.; Sun, J. P.; Lei, H. C.; et al. Double Superconducting Dome and Triple Enhancement of T_c in the Kagome Superconductor CsV_3Sb_5 under High Pressure. *Phys. Rev. Lett.* **2021**, *126* (24), No. 247001.
(40) Zheng, L.; Wu, Z.; Yang, Y.; Nie, L.; Shan, M.; Sun, K.; Song, D.; Yu, F.; Li, J.; Zhao, D.; et al. Emergent charge order in pressurized kagome superconductor CsV_3Sb_5. *Nature* **2022**, *611* (7937), 682−687.
(41) Di Salvo, F. J.; Moncton, D. E.; Wilson, J. A.; Mahajan, S. Coexistence of two charge-density waves of different symmetry in 4*Hb*-$TaSe_2$. *Phys. Rev. B* **1976**, *14* (4), 1543−1546.
(42) Friend, R. H.; Frindt, R. F.; Grant, A. J.; Yoffe, A. D.; Jerome, D. Electrical conductivity and charge density wave formation in 4*Hb*-TaS_2 under pressure. *J. Phys. Chem. Solids* **1977**, *10* (7), 1013.
(43) Garoche, P.; Manuel, P.; Veyssié, J. J.; Molinié, P. Dynamic measurements of the low-temperature specific heat of 2*H*-TaS_2 single crystals in magnetic fields. *J. Low Temp. Phys.* **1978**, *30* (3), 323−336.
(44) de la Barrera, S. C.; Sinko, M. R.; Gopalan, D. P.; Sivadas, N.; Seyler, K. L.; Watanabe, K.; Taniguchi, T.; Tsen, A. W.; Xu, X.; Xiao, D.; et al. Tuning Ising superconductivity with layer and spin−orbit coupling in two-dimensional transition-metal dichalcogenides. *Nat. Commun.* **2018**, *9* (1), 1427.
(45) Woollam, J. A.; Somoano, R. B.; O'Connor, P. Positive Curvature of the H_{c2}-versus-T_c Boundaries in Layered Superconductors. *Phys. Rev. B* **1974**, *32* (13), 712−714.
(46) Xu, S.; Gao, J.; Liu, Z.; Chen, K.; Yang, P.; Tian, S.; Gong, C.; Sun, J.; Xue, M.; Gouchi, J.; et al. Effects of disorder and hydrostatic pressure on charge density wave and superconductivity in 2*H*-TaS_2. *Phys. Rev. B* **2021**, *103* (22), No. 224509.
(47) Shibauchi, T.; Carrington, A.; Matsuda, Y. A Quantum Critical Point Lying Beneath the Superconducting Dome in Iron Pnictides. *Annu. Rev. Condens. Matter Phys.* **2014**, *5* (1), 113−135.
(48) Xiang, L.; Kaluarachchi, U. S.; Böhmer, A. E.; Taufour, V.; Tanatar, M. A.; Prozorov, R.; Bud'ko, S. L.; Canfield, P. C. Dome of magnetic order inside the nematic phase of sulfur-substituted FeSe under pressure. *Phys. Rev. B* **2017**, *96* (2), No. 024511.
(49) Chen, G. P.; Bykova, E.; Bykov, M.; Edmund, E.; Cao, Z.-Y.; Chen, X.-J.; Smith, J. S.; Chariton, S.; Prakapenka, V. B.; Goncharov, A. F. Structural and vibrational behavior of 2*H*-$NbSe_2$ at high pressures. *Phys. Rev. B* **2022**, *105* (22), No. 224114.
(50) Zhou, Y.; Chen, C.; Zhou, Y.; Chen, X.; Gu, C.; An, C.; Zhang, B.; Yuan, Y.; Wu, H.; Zhang, R.; et al. Pressure-induced evolution of structural and electronic properties in $TiTe_2$. *Phys. Rev. B* **2019**, *99* (12), No. 125104.
(51) Sereika, R.; Park, C.; Kenney-Benson, C.; Bandaru, S.; English, N. J.; Yin, Q.; Lei, H.; Chen, N.; Sun, C. J.; Heald, S. M.; et al. Novel Superstructure-Phase Two-Dimensional Material 1*T*-VSe_2 at High Pressure. *J. Phys. Chem. Lett.* **2020**, *11* (2), 380−386.
(52) Birch, F. Finite Elastic Strain of Cubic Crystals. *Phys. Rev. J.* **1947**, *71* (11), 809−824.
(53) Rajaji, V.; Dutta, U.; Sreeparvathy, P. C.; Sarma, S. C.; Sorb, Y. A.; Joseph, B.; Sahoo, S.; Peter, S. C.; Kanchana, V.; Narayana, C. Structural, vibrational, and electrical properties of 1*T*-$TiTe_2$ under hydrostatic pressure: Experiments and theory. *Phys. Rev. B* **2018**, *97* (8), No. 085107.
(54) Tonjes, W. C.; Greanya, V. A.; Liu, R.; Olson, C. G.; Molinié, P. Charge-density-wave mechanism in the 2*H*-$NbSe_2$ family: Angle-resolved photoemission studies. *Phys. Rev. B* **2001**, *63* (23), No. 235101.
(55) Zhu, X.; Cao, Y.; Zhang, J.; Plummer, E. W.; Guo, J. Classification of charge density waves based on their nature. *Proc. Natl. Acad. Sci. U.S.A.* **2015**, *112* (8), 2367−2371.
(56) Johannes, M. D.; Mazin, I. I. Fermi surface nesting and the origin of charge density waves in metals. *Phys. Rev. B* **2008**, *77* (16), No. 165135.
(57) Zhu, X.; Guo, J.; Zhang, J.; Plummer, E. W. Misconceptions associated with the origin of charge density waves. *Adv. Phys. X* **2017**, *2* (3), 622−640.
(58) Kvashnin, Y.; VanGennep, D.; Mito, M.; Medvedev, S. A.; Thiyagarajan, R.; Karis, O.; Vasiliev, A. N.; Eriksson, O.; Abdel-Hafiez, M. Coexistence of Superconductivity and Charge Density Waves in Tantalum Disulfide: Experiment and Theory. *Phys. Rev. Lett.* **2020**, *125* (18), No. 186401.
(59) Ravy, S.; Laulhé, C.; Itié, J.-P.; Fertey, P.; Corraze, B.; Salmon, S.; Cario, L. High-pressure X-ray diffraction study of 1*T*-TaS_2. *Physica B Condens. Matter.* **2012**, *407* (11), 1704−1706.

https://doi.org/10.1021/acs.nanolett.4c00579
Nano Lett. 2024, 24, 6002−6009